J|A|C|S
ARTICLES
Published on Web 12/21/2002

Silicalite Crystal Growth Investigated by Atomic Force Microscopy

Jonathan R. Agger,* Noreen Hanif, Colin S. Cundy, Andrew P. Wade, Sally Dennison, Paul A. Rawlinson, and Michael W. Anderson*

Contribution from the UMIST Centre for Microporous Materials, P.O. Box 88, Manchester M60 1QD, U.K.

Received June 28, 2002; E-mail: j.agger@umist.ac.uk

Abstract: Atomic force microscopy has been used to image the various facets of two morphologically distinct samples of silicalite. The smaller (20 μm) sample A crystals show 1 nm high radial growth terraces. The larger (240 μm) sample B crystals show growth terraces 1 to 2 orders of magnitude higher than the terraces on sample A with growth edges parallel to the crystallographic axes. Moreover, the terraces on the (010) face are significantly higher than the terraces on the (100) face − inconsistent with the previously proposed 90° intergrowth structure. Sample A highlights that under certain synthetic conditions, silicalite grows in a manner akin to zeolites Y and A, via the deposition of layers comprising, in the case of silicalite, pentasil chains. It is probable that the rate of terrace advance is identical on the (010) and (100) faces, and it is the rate of terrace nucleation that dictates the overall growth rate of each facet and hence the relative size expressed in the final crystal morphology. Analysis of the growth terraces of sample B and detailed consideration of the structures of both MFI, and a closely related material MEL, lead to the proposal of a generalized growth mechanism for silicalite including the incorporation of defects within the structure. These defects are thought to be responsible for both the relative and the absolute terrace heights observed and may also explain the hourglass phenomenon observed by optical microscopy. The implications of this growth mechanism, supported by results of infrared microscopy, generate a new dimension to the continuing debate on the existence of intergrowths within one of the most important structures relevant to zeolite catalysis.

Introduction

Because of high internal surface area, the zeolite class of solid acids has found many large-scale uses in industry, including petroleum cracking, water softening, shape-selective catalysis, and gas separation, with possible future applications in nanocomposite electronic devices. However, despite their initial discovery dating back to 1789, our understanding of zeolite crystal growth mechanisms remains limited.

One way to study crystal growth is to observe the exposed facets of a crystal. Until very recently, SEM techniques portrayed the surface of synthetic zeolite crystals as being effectively smooth, although certain materials exhibit large superposed surface features. However, a very recent development using field emission gun SEM in conjunction with chromium sample coating to increase the secondary electron yield has produced beautiful images of nanometer scale terraces on the surface of zeolites A, X, and silicalite.[1] This technique allows for rapid characterization because of the ability to simultaneously image multiple crystallites, although direct step height quantification is not possible. The nonconducting nature of zeolite crystals precludes the use of scanning tunneling microscopy (STM) in vacuo; however, images have been obtained under ambient conditions.[2] High-resolution transmission electron microscopy (HRTEM) yields extremely detailed surface step images, but only in cross-section.[3] Further development of scanning probe microscopy (SPM) led to the advent of atomic force microscopy (AFM)[4] that now enables very high-resolution imaging of nonconducting surfaces with the ability to measure the height of the surface very accurately. At an order of magnitude below the maximum resolution attainable with such a microscope, zeolite growth features are observed, providing a wealth of information on the processes by which surface propagation occurs.

AFM was first used to image the surface of a zeolite in 1990. Weisenhorn et al. reported imaging of the cleaved (010) face of clinoptilolite under water, *tert*-butyl alcohol, and dilute *tert*-butylammonium chloride solution.[5] Further studies of mineral zeolites include scolecite,[6,7] stilbite,[6−8] faujasite,[6,7] heulandite,[8−11]

(1) Bazzana, S.; Dumrul, S.; Warzywoda, J.; Hsiao, L.; Klass, L.; Knapp, M.; Rains, J. A.; Stein, E. M.; Sullivan, M. J.; West, C. M.; Woo, J. Y.; Sacco, A., Jr. In *Proc. 2nd Int. FEZA Conf., Taormina*; Aiello, R., Giordano, G., Testa, F., Eds.; Elsevier: New York, 2002; 142A, pp 117−124.

(2) Jansen, J. C.; Schoonman, J.; van Bekkum, H.; Pinet, V. *Zeolites* **1991**, *11*, 306−307.

(3) Oshuna, T.; Terasaki, O.; Alfredsson, V.; Bovin, J.-O.; Watanabe, D.; Carr, S. W.; Anderson, M. W. *Proc. R. Soc. London, Ser. A* **1996**, *452*, 715−740.

(4) Binnig, G.; Quate, C. F.; Gerber, C. *Phys. Rev. Lett.* **1986**, *56*, 930−933.

(5) Weisenhorn, A. L.; MacDougall, J. E.; Gould, S. A. C.; Cox, S. D.; Wise, W. S.; Massie, J.; Maivald, P.; Elings, V. B.; Stucky, G. D.; Hansma, P. K. *Science* **1990**, *247*, 1330−1333.

(6) MacDougall, J. E.; Cox, S. D.; Stucky, G. D.; Weisenhorn, A. L.; Hansma, P. K.; Wise, W. S. *Zeolites* **1991**, *11*, 429−433.

10.1021/ja020899f CCC: $25.00

and mordenite.[12] These investigations largely comprise imaging of cleaved surfaces to reveal the underlying structure both at a molecular scale and at lower resolution to indirectly determine growth features by observing preferential cleavage.

Initial AFM images of the surface of a synthetic zeolite were published in 1996.[13] Work performed on synthetic zeolite crystals to date[1,13−21] suggests growth occurs via the deposition and subsequent expansion of layers. Layer height typically corresponds to some easily identifiable element of the structure. Layers advance by addition of nutrient at ledges and kinks in ledges in such a manner that the area of each layer is proportional to the time for which that layer has been growing. Computer simulation of the growth of zeolite A allowed the first ever estimation of probabilities for attachment of gel nutrient at different types of site on the surface of a zeolite.[20] Two recent review articles summarize current progress toward the elucidation of zeolite growth by means of AFM.[22,23]

The motivation for this current study lay in the intriguing nature of very high terraces (up to 110 nm) observed on the surface of silicalite. Clearly, such terraces are not related to any aspect of the unit cell. This work details a mechanism for the creation of such oversized terraces, caused by defect incorporation into the crystal structure during growth. It is suggested that these defects are crucial to understanding the origin of the "hourglass" optical phenomenon observed in silicalite crystals imaged under cross polarizing lenses.[24−27] There are also important ramifications for the ongoing debate into the existence of 90° intergrowths within silicalite.

Improved understanding of zeolite growth should enable a more targeted approach to zeolite synthesis in the future and may ultimately lead to the possibility of zeolite design to order. Understanding of defect incorporation has ramifications on diffusion control within zeolites and may lead to control over the location and degree of defect inclusion.

Experimental Section

Preparation of Silicalite Sample A. First, 205 g of tetraethyl orthosilicate (BDH GPR) was added to a solution of 27.1 g of tetrapropylammonium (TPA) bromide (Fluka purum) and 4.0 g of sodium hydroxide (BDH AR) in 1770 g of deionized water in a polypropylene container. The vessel was then sealed, and the two-phase mixture was stirred at room temperature until the organic layer had reacted completely to give a clear, homogeneous solution (ca. 48 h). The molar compositional ratio of the resulting mixture was 0.10TPABr: SiO_2:0.05Na_2O:4.00EtOH: 98H_2O.

Next, 600 g of the above mixture in a polypropylene bottle was aged in a thermostat bath at 50 °C for 7 days. Subsequently, the mixture was placed in a 1 L stainless steel autoclave and heated at 130 °C for 48 h, stirring at 300 rpm. The (stirred) autoclave was then allowed to cool, and the product was isolated by centrifugation, washed thoroughly four times with water, and oven dried at 105 °C.

Preparation of Silicalite Samples B1 and B2. These samples were prepared by similar methods in different laboratories. Silicalite B1 was prepared as follows: 1.77 g of tetrapropylammonium bromide was dissolved in 6.63 g of deionized water. To this solution was added 13.44 g of a 28% aqueous solution of ammonia followed by 5.31 g of LUDOX AS-40 colloidal silica. The resulting hazy solution was stirred for 3 h at room temperature. The solution was transferred to a Teflon-lined autoclave and heated at 180 °C for 3 days. The crystals were recovered by filtration, washed with 500 cm^3 of deionized water, rinsed with acetone, and then air-dry sonicated for 2 min to isolate the large crystals from any amorphous material. The gel composition was 0.19TPABr:SiO_2:6.25NH_4OH:24.4H_2O. Silicalite B2 was prepared according to method (V) in the paper by Müller and Unger.[28] Synthesis time and temperature were 7 days and 180 °C, with a gel composition of 0.14TPABr:SiO_2:4.17NH_4OH:36.6H_2O.

Scanning Electron Microscopy (SEM). Micrographs were obtained using a Philips XL30 instrument with field emission gun. Samples were prepared by dusting the silicalite powder onto double-sided carbon tape, mounted on a metal stub. The sample was subsequently sputter coated with a thin carbon film to reduce charging effects.

Atomic Force Microscopy (AFM). AFM images were recorded on a Digital Instruments Nanoscope III Multimode microscope operating in TappingMode. This differs from contact-mode AFM in that the cantilever is excited into resonant oscillation by means of a piezoelectric driver. The oscillation amplitude is used as a feedback signal to measure topographic variations of the sample. In the associated technique of phase imaging, the phase lag of the cantilever oscillation, relative to the signal sent to the cantilever's piezo driver, is simultaneously monitored. Phase lag as applied to zeolite imaging serves to enhance growth-layer edges. AFM sample preparation methodology is published elsewhere.[15] First-order *xy* planefitting (equivalent to projecting the image onto a horizontal plane) has been employed to level crystal terraces.

Optical Microscopy. Optical micrographs were recorded on dry samples using a Leitz (Laborlux 12 Pol) polarizing microscope and Agfa CT100 color film.

Infrared Microscopy. Infrared microscopy was performed on a Nicolet Nic-Plan infrared microscope coupled to a Nicolet Magna-IR 550 spectrometer. The crystals were sprinkled onto a barium fluoride disk that was then inserted into an environmental cell. Calcination of the crystals was achieved by heating them to 500 °C at a rate of 1 °C min^{-1} under flowing nitrogen (100 mL min^{-1}). They were held at this temperature for 24 h, the atmosphere being switched to oxygen (100 mL min^{-1}) for the final 12 h. The temperature was then ramped down to 150 °C again at a rate of 1 °C min^{-1}, again under flowing nitrogen (100 mL min^{-1}). The spot size was set to 60 × 60 μm^2 by means of the upper aperture. The crystals were maneuvered under the beam by

(7) Occelli, M. L.; Gould, S. A. C.; Stucky, G. D. *Stud. Surf. Sci. Catal*. **1994**, *84*, 485−492.
(8) Komiyama, M.; Yashima, T. *Jpn. J. Appl. Phys.* **1994**, *33*, 3761.
(9) Scandella, L.; Kruse, N.; Prins, R. *Surf. Sci. Lett.* **1993**, *281*, 331−334.
(10) Binder, G.; Scandella, L.; Schumacher, A.; Kruse, N.; Prins, R. *Zeolites* **1996**, *16*, 2−6.
(11) Yamamoto, S.; Sugiyama, S.; Matsuoka, O.; Kohmura, K.; Honda, T.; Banno, Y.; Nozoye, H. *J. Phys. Chem.* **1996**, *100*, 18474−18482.
(12) Yamamoto, S.; Matsuoka, O.; Sugiyama, S.; Honda, T.; Banno, Y.; Nozoye, H. *Chem. Phys. Lett.* **1996**, *260*, 208−214.
(13) Anderson, M. W.; Agger, J. R.; Thornton, J. T.; Forsyth, N. *Angew. Chem., Int. Ed. Engl.* **1996**, *35*, 1211−1213.
(14) Sugiyama, S.; Yamamoto, S.; Matsuoka, O.; Honda, T.; Nozoye, H.; Qiu, S.; Yu, J.; Terasaki, O. *Surf. Sci.* **1997**, *377*, 140−144.
(15) Agger, J. R.; Pervaiz, N.; Cheetham, A. K.; Anderson, M. W. *J. Am. Chem. Soc.* **1998**, *120*, 10754−10759.
(16) Anderson, M. W.; Agger, J. R.; Pervaiz, N.; Weigel, S. J.; Cheetham, A. K. In *Proc. 12th Int. Zeol. Conf., Baltimore*; Treacy, M. M. J., Marcus, B. K., Bisher, M. E., Higgins, J. B., Eds.; MRS, 1998; pp 1487−1494.
(17) Sugiyama, S.; Yamamoto, S.; Matsuoka, O.; Nozoye, H.; Yu, J.; Zhu, G.; Qiu, S.; Terasaki, O. *Microporous Mesoporous Mater.* **1999**, *28*, 1−7.
(18) Warzywoda, J.; Valcheva-Traykova, M.; Rossetti, G. A., Jr.; Baç, N.; Joesten, R.; Suib, S. L.; Sacco, A., Jr. *J. Cryst. Growth* **2000**, *220*, 150−160.
(19) Anderson, M. W.; Hanif, N.; Agger, J. R.; Chen, C.-Y.; Zones, S. I. In *Stud. Surf. Sci. Catal.*; Galerneau, A., Di Renzo, F., Fajula, F., Vedrine, J., Eds.; Elsevier: Amsterdam, 2001; p 141.
(20) Agger, J. R.; Hanif, N.; Anderson, M. W. *Angew. Chem., Int. Ed.* **2001**, *40*, 4065−4067.
(21) Dumrul, S.; Bazzana, S.; Warzywoda, J.; Biederman, R. R.; Sacco, A., Jr. *Microporous Mesoporous Mater.* **2002**, *54*, 79−88.
(22) Anderson, M. W.; Agger, J. R. *Solid State Sci.* **2001**, *3*, 809−819.
(23) Anderson, M. W. *Curr. Opin. Solid State Mater. Sci.* **2001**, *5*, 407−415.
(24) Weidenthaler, C.; Fischer, R. X.; Shannon, R. D. *J. Phys. Chem.* **1994**, *98*, 12687−12694.
(25) Price, G. D.; Pluth, J. J.; Smith, J. V.; Bennett, J. M.; Patton, R. L. *J. Am. Chem. Soc.* **1982**, *104*, 5971−5977.
(26) Hay, D. G.; Jaeger, H.; Wilshier, K. G. *Zeolites* **1990**, *10*, 571−576.
(27) Geus, E. R.; Jansen, J. C.; van Bekkum, H. *Zeolites* **1994**, *14*, 82−88.
(28) Müller, U.; Unger, K. K. *Zeolites* **1988**, *8*, 154.

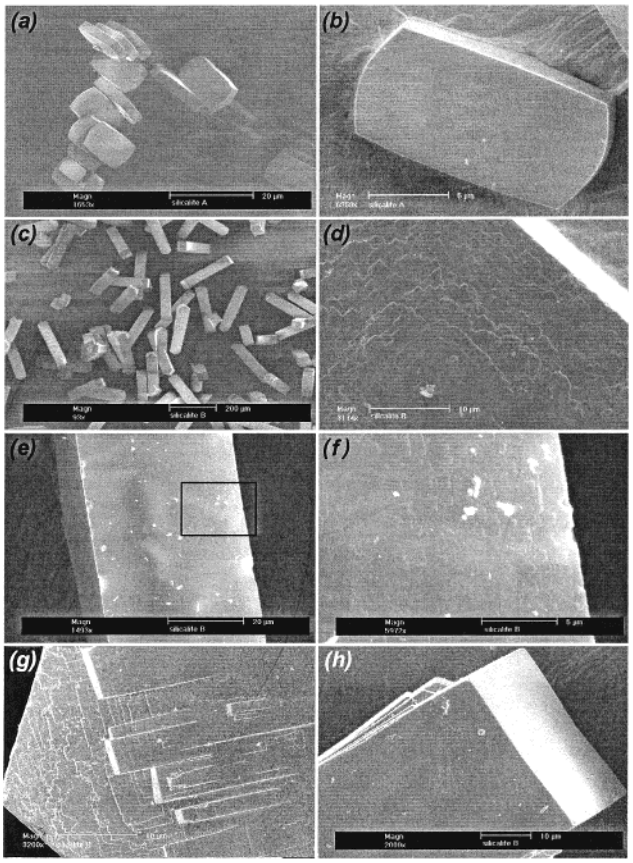

Figure 1. Various scanning electron micrographs of silicalite samples A and B: (a) sample A crystals; (b) individual sample A crystal showing the (010) face; (c) sample B1 crystals; (d) terraces visible by SEM on the (010) face of sample B1; (e) a (100) face of sample B1; (f) magnified image of the rectangular area shown in figure (e); (g) a (010) face of sample B1 showing ramps and terraces; (h) side view of the ramps shown in (g).

means of a moving sample stage. Spectra were recorded with a resolution of 16 cm^{-1} and 2048 scans.

Results

Crystal morphology of the three silicalite samples was compared using scanning electron microscopy. Silicalite A comprises well-formed crystals, with uniform "rounded-boat" shape morphology, ranging in size from $20 \times 8 \times 2$ to $10 \times 5 \times 1$ μm^3, as shown in Figure 1a. Figure 1b shows the smooth appearance of the crystal surfaces at the resolution of this microscope.

Silicalites B1 and B2 comprise much larger crystals with "classic-boat" shape morphology and a size distribution of ca. $240 \times 60 \times 40$ μm^3, as shown in Figure 1c. In contrast, the surfaces of these crystals are highly detailed. Figure 1d shows part of the (010) face. An array of high terraces may be seen on the surface. Figure 1e shows the central portion of a (100) face. Again, an array of high terraces may be seen on the surface, growing toward the edge of the face. This is shown more clearly in Figure 1f in which the area delineated by the rectangle in Figure 1e is shown at greater magnification. Many crystals exhibit wedge-shaped features toward the extremities of the (010) face as shown in Figure 1g and h which were taken approximately along the [010] and [100] directions, respectively.

AFM was used to perform a detailed surface study of both silicalite samples. Under the scanning electron microscope, the

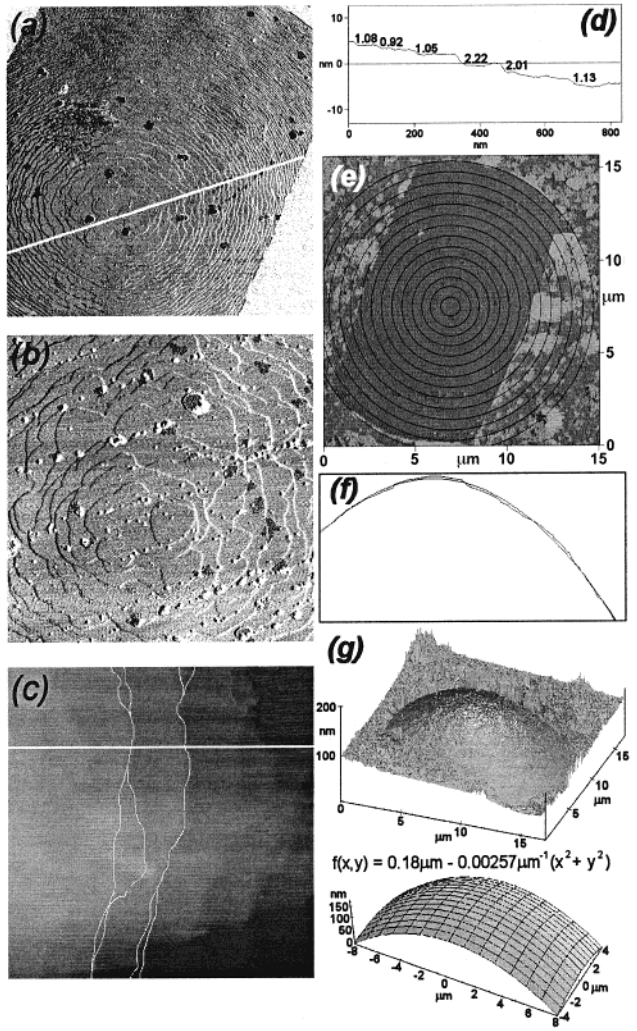

Figure 2. AFM images of a (010) face of sample A: (a) phase image 8.8 $\times$ 8.8 μm^2; (b) phase image 3.5 $\times$ 3.5 μm^2; (c) height image 830 $\times$ 830 nm^2. (d) Section analysis recorded along the white line in (c). (e) The circular habit of the rounded ends of the crystal. (f) Parabolic cross-section, taken along the white line in (a). (g) 3D plot and corresponding analytical surface.

(010) faces of silicalite sample A appeared smooth. However, the atomic force microscope reveals the existence of a multitude of 1.0 nm high terraces. The terraces show no preferential growth direction; consequently, over time, growth fronts develop an approximately circular profile. They are concentric, radiating out to the crystal edge from either one or a small number of central nucleation points, as shown in Figure 2a. Closer examination of a (010) face reveals the degree of terrace irregularity as shown in Figure 2b. Terrace irregularity and edge proximity cause frequent merging with the creation of double-height ledges, highlighted in white in Figure 2c. Merging increases toward the edge of the crystal. The section analysis of Figure 2c, given in Figure 2d, reveals terrace height to be either 1.0 ± 0.1 or 2.0 ± 0.1 nm. Errors were determined from the measurement of over 100 heights. The double-height ledges coincide exactly with terrace merging. The rounded ends of the crystal perfectly match the circular profile of the advancing terrace fronts as shown in Figure 2e. It should be noted that the discrepancy on the lower edge is due to the crystal having sunk slightly into the thermoplastic fixative.

The separation between consecutive terraces is observed to decrease moving away from the center of the crystal face. More accurately, any cross-section taken through the apex of the surface is parabolic in profile. This is highlighted in Figure 2f, which shows a section, taken along the randomly chosen white line shown in Figure 2a, with a parabola fitted to the profile. The parabola matches the section very closely. In three dimensions, the growing face approximates to the surface defined by the following equation:

$$f(x,y) = 0.18\mu\text{m} - 0.00257\mu\text{m}^{-1}(x^2 + y^2) \qquad (1)$$

Figure 2g shows comparative images of the surfaces of the actual crystal and the function.

Figure 3a shows an $11.8 \times 11.8\ \mu\text{m}^2$ AFM image of a (100) face. The image highlights the 1 nm high terraces similar to those observed in Figure 2a. Section analysis along the [001] direction, Figure 3b, yields a parabolic profile corresponding to the equation:

$$f(x) = 0.325\ \mu\text{m} - 0.00871\ \mu\text{m}^{-1}(x^2) \qquad (2)$$

Figure 3c−e depicts AFM phase images of a typical intergrowth on the (010) surface of sample A. The circular terraces on the (010) face, radiating out toward the edge of the crystal, can clearly be seen in Figure 3e. The intergrowth comprises multiple facets, the highest of which rises 758 nm above the height of the (010) face, as shown in the section analysis in Figure 3f, inset, the height image with white line along which the section was recorded.

The section of the end of the intergrowth, highlighted with an asterisk in Figure 3c, is a circular arc, evidenced by the inset of Figure 3f, in which the cross-section has been scribed onto a circle. Although the inset is necessarily small, the fit prior to reduction is excellent.

Terraces similar to those observed on both the (010) and the (100) faces are evident on the intergrowth facets. Sections taken through the apexes are parabolic. Figure 3g shows two parabolic sections: the lower curve is that of the largest intergrowth facet; the upper curve is that of the underlying (010) face. The intergrowth section approximates to the parabola defined by the following equation:

$$f(x) = 0.034\ \mu\text{m} - 0.0100\ \mu m^{-1}(x^2) \qquad (3)$$

It rises approximately 34 nm across its 3.5 μm length. The parabolic section of the underlying (010) face rises approximately 180 nm across its 16 μm length. Figure 3h shows the same parabolae with modified constants such that the height of the intergrowth parabola is 4 times that of the underlying (010) face parabola.

The terraces on the intergrowth are noncommensurate with the terraces on the underlying face. Compensation for the existence of the intergrowth, evidenced by perturbation of the regular circular terrace profile, is observed.

The atomic force micrograph of a (010) face of silicalite sample B1, given in Figure 4a, in contrast to that of sample A, shows an array of terraces uniformly growing toward the edge of the crystal. The terrace fronts lie parallel to the crystal edge. Exhaustive section analysis across this image reveals that terrace step heights lie in the range of ca. 30−110 nm − up to 2 orders of magnitude higher than the radial terraces observed on the

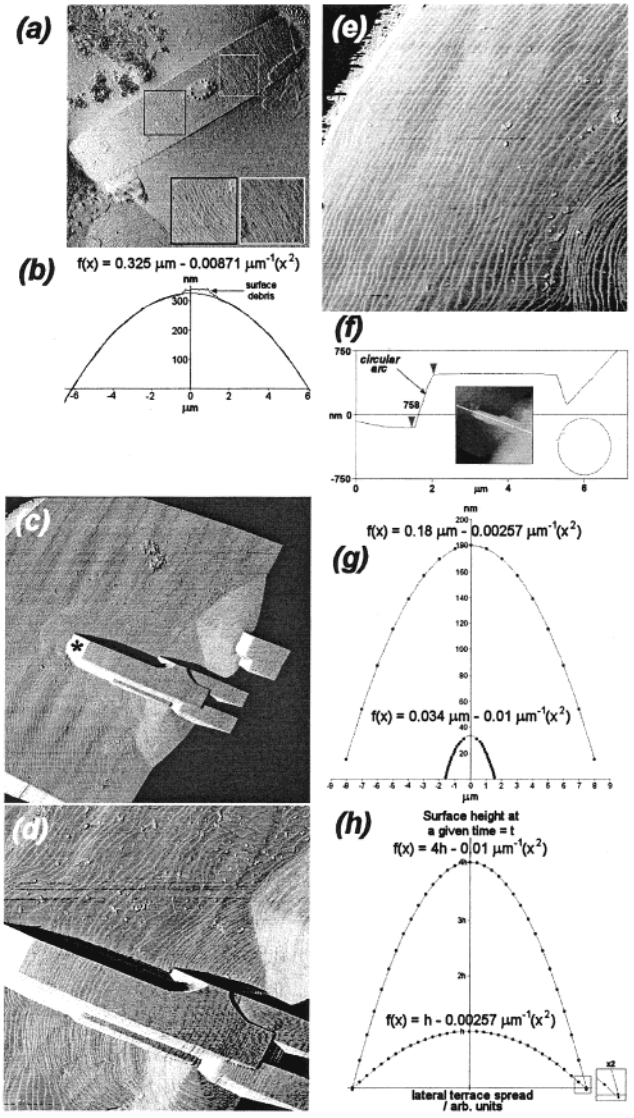

Figure 3. (a) An $11.8 \times 11.8\ \mu\text{m}^2$ AFM amplitude image of a (100) face of sample A. Inset: two areas of the image magnified to better highlight the terraces. (b) Parabolic section from the corresponding height image, taken along the [001] axis of the crystal and the quadratic equation. (c−e) Series of AFM phase images of intergrowth on the (010) face of sample A: 8.0×8.0, 4.0×4.0, and $2.6 \times 2.6\ \mu\text{m}^2$, respectively. (f) The section analysis of the inset height image of the intergrowth along the white line. Part of the section has been scribed onto a circle to highlight the circular nature of the end of the intergrowth; this is also shown in the inset. (g) Parabolic cross-sections, taken along [001] of a (010) face (upper curve) and an intergrowth on the (010) face (lower curve) of sample A. The corresponding analytical quadratics are shown. (h) The same parabolae redrawn such that their apexes cross the height axis at h and $4h$. Note that the positions of the parabolae are inverted between (g) and (h).

(010) face of sample A. A typical section is shown in the figure below the image. The micrograph of the (100) face, Figure 4b, also shows terraces growing uniformly toward the edge of the crystal. The section, shown below the image, reveals terrace step heights in the range of ca. 6−20 nm − significantly smaller than that on the (010) face, yet approximately an order of magnitude higher than the terraces observed on sample A. Terraces, similar to those observed on silicalite B1 crystals, are also observed on silicalite B2 crystals.

Figure 5a shows an optical micrograph of silicalite sample B1. Figure 5b shows the same image taken under cross-polars

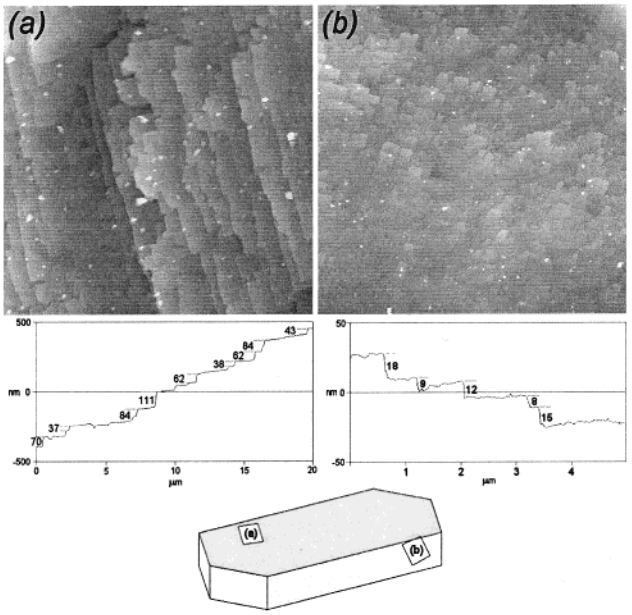

Figure 4. 20 × 20 μm^2 AFM height images of (a) the (010) face; (b) the (100) face of sample B1. Typical section analyses of the two faces are also given, and the lower figure reveals image orientation.

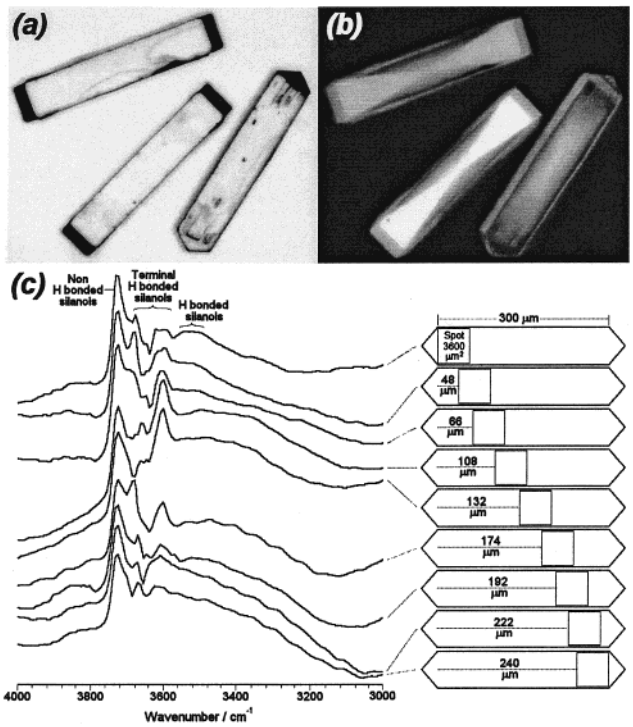

Figure 5. (a) Optical micrograph of silicalite sample B1 crystals and (b) the same image taken under cross-polars. (c) A series of FT-IR spectra taken with a 60 × 60 μm^2 spot focused on the (010) face of silicalite B2 at successive positions along the [001] direction.

− all crystals exhibit the hourglass, although the phenomenon is clearer in crystals lying on their (100) faces. Careful inspection of the hourglass reveals the curved nature of the interface. This phenomenon is equally observed in silicalite B2 crystals.

Figure 5c shows a series of infrared spectra, recorded with a 60 × 60 μm^2 spot size focused on the (010) face of sample B2, taken at different positions along the [001] direction. The spectrum obtained from the left extremity of the crystal agrees well with previously published work exhibiting three narrow signals at 3730, 3691, and 3612 cm^{-1} and a further broad signal at 3531 cm^{-1}.[29,30] As the infrared beam traverses the sample, a generally symmetrical trend of change may be observed. Toward the middle of the face, there is a decrease in the signal at 3730 cm^{-1}, an increase and shifting of the signal at 3691 cm^{-1}, and a strong increase in the signal at 3612 cm^{-1}.

Discussion

SEM reveals that the silicalite samples exhibit very different crystal morphologies. Sample A comprises relatively small, rounded-boat shaped crystals with smooth surfaces and limited instances of intergrowth, while samples B1 and B2 comprise large, classic-boat shaped crystals with much surface detail. The origin of these differences undoubtedly lies in the different synthetic procedures used to produce the crystals. The smoother sample A crystals were synthesized in a stirred Na^+, TPA reaction medium at a temperature 50 °C below that of the rougher NH_4^+, TPA sample B crystals.

The contrast in crystal morphology is amplified by AFM. The terraces observed on the (010) face of sample A are consistent with the literature.[13−15] They are uniformly 1.0 nm in height, corresponding to the thickness of the pentasil chains measured along [010], shown in Figure 6a, that make up the MFI structure. The parabolic nature of the cross-section, similar to that observed for zeolites A[1,15,21] and Y,[13] implies that the area of a terrace is proportional to elapsed growth time. This observation might, at first, appear to contradict the macroscopic phenomena of crystal growth; linear growth rates for batch-synthesized zeolites tend to be constant, or nearly so, over the majority of the growth period.[31] It thus follows that, under such conditions, the area of a crystal face is proportional to the *square* of the elapsed growth time. However, terrace advancement rates are far greater in the lateral plane than they are in the plane perpendicular to it, and if we accept that the rate-limiting process for the advancement of a crystal face is the nucleation of successive layers, then there is no direct link with the lateral terrace spreading rate in the overall kinetics.

A second point must also be raised, although its effect is currently not fully resolved. At the end of the synthesis reaction, there is an appreciable period over which the crystal linear growth rate dies away to zero as nutrient is exhausted and supersaturation falls. Because nucleation is a more sensitive function of supersaturation than is growth rate, the falling supersaturation would be expected to cause a larger rate decrease in surface nucleation than in layer spreading, causing a successive increase in terrace spacing toward the center of the face. Assuming that the deceleration period corresponds to ca. 20% of the total crystal radial increase, we then find that this final growth will account for ca. 50% of the crystal mass and essentially the entire external surface which is being examined microscopically. Earlier growth patterns, including the entire period of steady-state growth, are hidden within the body of the crystal.

The approximately circular habit of the terraces suggests a degree of parity between the individual growth rates at a terrace

(29) Zecchina, A.; Bordiga, S.; Spoto, G.; Scarano, D.; Petrini, G.; Leofanti, G.; Padovan, M.; Otero Areàn, C. *J. Chem. Soc., Faraday Trans.* **1992**, *88*, 2959−2969.
(30) Astorino, E.; Peri, J. B.; Willey, R. J.; Busca, G. *J. Catal.* **1995**, *157*, 482−500.
(31) Barrer, R. M. *Hydrothermal Chemistry of Zeolites*; Academic Press: London, 1982; p 133.

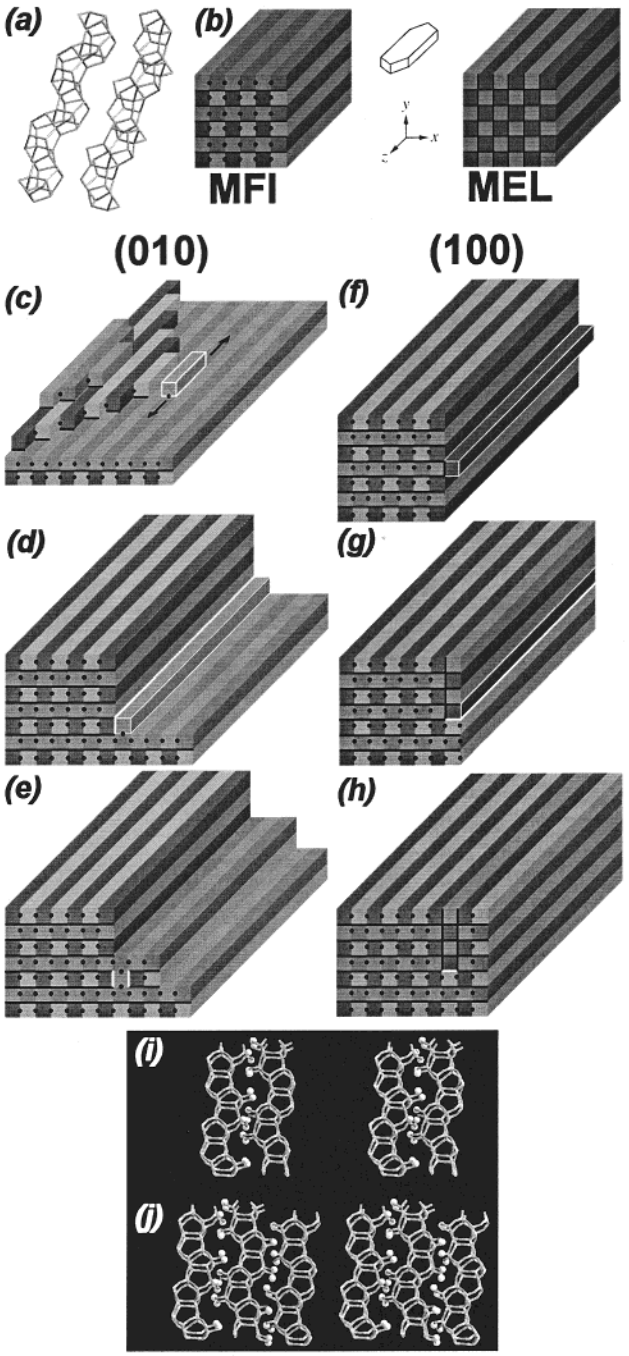

Figure 6. (a) Enantiomeric pair of pentasil chains; (b) schematic representation of the structures of MFI and MEL; (c−e) formation mechanism of terraces on the (010) face of sample B; (f−h) formation mechanism of terraces on the (100) face of sample B; (i, j) pairs of stereoprojections of a single and back-to-back double defect, respectively.

front and at a kink in a terrace front. Dominant kink growth would result in blocking out of the terraces and an overall rectilinear habit as is observed in the growth of zeolite A.

Features observed on the (010) face of silicalite sample A, such as those shown in Figure 3c, are frequently suggested to be 90° intergrowths in the literature.[24−27] There are five pieces of evidence from this current work to support this view in the case of silicalite sample A crystals. First, the terraces observed on the top facet of the intergrowth are similar to those observed on the (100) faces of the crystal; however, they are also similar to those on the (010) faces. Second, the end of the intergrowth has a circular profile, similar to the profile of the end of the crystal, but rotated by 90° around [001]. Third, the perturbation of the circular terraces on the (010) face around the intergrowth suggests it is embedded within the crystal in agreement with a study by Hay et al.[26] in which they dislodged 90° silicalite intergrowth components. Fourth, the ratio of areas of the (010) and (100) facets is ca. 4:1, implying a 4-fold ratio in their growth rates − the (010) face being the slower growing. The [001] parabolic sections of the (010) and purported (100) intergrowth faces, shown in Figure 3g, permit analysis of growth rates on the two faces. Assumption of a 4-fold higher rate of nucleation on the (100) face than that on the (010) face, based on the overall crystal morphology, places the apex of the intergrowth parabola 4 times higher than the apex of the (010) face parabola. This is shown in Figure 3h, the arbitrary heights being 4*h* and *h*. The two parabolae then intersect the zero height axis contiguously; see the doubly magnified inset on the right of the figure. This is strong evidence that the intergrowth face is a (100) face, but it further implies the conclusion of the same rate of terrace spread on both faces. Fifth, the quadratic constants for the (100) and purported (100) intergrowth faces are similar, being 0.00871 and 0.0100 μm^{-1}, respectively. The discrepancy is small considering the two constants are necessarily measured from two distinct crystals. Explanation of the difference in nucleation rates and the similarity in terrace spreading rates necessitates an understanding of the structure of MFI. This is developed in the following discussion of the relative terrace heights observed on the facets of the two silicalite samples.

Crystallization terraces, observed on the surface of microporous materials, generally possess heights related to some aspect of the known structure of the material, as observed in this present study on the (010) and (100) faces of silicalite sample A. This implies that, at least under certain synthetic conditions, silicalite seems to grow via a simple layer mechanism. However, the high terraces imaged on the (010) and (100) faces of silicalite samples B1 and B2, up to 110 and 20 nm, respectively, are up to 2 orders of magnitude larger than the unit cell parameters for silicalite.

Explanation of this apparent anomaly necessitates detailed consideration of not only the structure of MFI, but also that of MEL. In effect, both structures are generated from the same basic building units, applying different symmetry constraints.[32] The building units are an enantiomeric pair of chiral pentasil chains, shown in Figure 6a. To generate either structure, as shown in Figure 6b, the pentasil chains (depicted as blocks) must be oriented along [001]. Connectivity dictates that the chains must be stacked with alternating chirality in both the [100] and the [010] directions. This is highlighted by means of alternating light and dark blocks. However, successive chains may be related by either a mirror plane or an inversion center. Along [010], successive chains are related by mirror planes, depicted in the figure as black lines. Along [100], successive pairs are related either by mirror planes, generating MEL structure, or by inversion centers, depicted in the figure as black dots, generating MFI structure. No other faultless three-dimensional connectivity is possible. Other connectivities lead to structural defects, and therein lies the key to understanding

(32) Ohsuna, T.; Terasaki, O.; Nakagawa, Y.; Zones, S. I.; Hiraga, K. *J. Phys. Chem. B* **1997**, *101*, 9881.

the high terraces observed on the surface of silicalite sample B.

The following discussion should be read in conjunction with a study by Ohsuna et al. concerning faulted nucleation in B-MEL,[32] as the nucleation processes and subsequent defects proposed in this work are similar to those proposed in that study.

Figure 6c depicts a model of the (010) face of a silicalite crystal. Terrace fronts of the top two layers are shown, growing outward in a radial pattern. Suppose a surface nucleation occurs with inversion symmetry rather than the preferred mirror symmetry, represented in the figure by the small block highlighted in white. Although full connectivity to the layer below via inversion symmetry is possible, subsequent connectivity to any part of the bulk structure via the {100} faces is now impossible. Because of this, such a nucleation may only propagate along [001], indicated by the black arrows. Growth of this nucleation results in a lateral barrier to the radial progression of the MFI structure, resulting in a piling up of the layers, as depicted in Figure 6d. The resulting defect at the base, shown by the thick white line, comprises interpenetrating, dangling silanol bonds alternating from the two pentasil chains flanking the defect, as shown in Figure 6i.

Notwithstanding this defect, it is possible for the structure to recover as depicted in Figure 6e. Nucleation of a further pentasil chain with inversion symmetry regenerates the three-dimensional connectivity. Once buried, each side of the defect is lined by a layer of interpenetrating, dangling silanol groups, depicted as thick white lines in Figure 6e and shown in Figure 6j. Such a defect could be responsible for the up to 110 nm high terraces observed on the (010) face. Similar reasoning can be used to explain the up to 20 nm high terraces on the (100) face.

Suppose a pentasil chain nucleates on the (100) face with mirror symmetry rather than inversion symmetry, as depicted in Figure 6f. Again, this creates a structural defect because advancing terraces cannot link to either {010} face as depicted by the thick white line shown in Figure 6g. Once again, this will result in a pile up of terraces. Connectivity may be recovered by switching to the MEL structure. As Figure 6h shows, extended growth of MEL curtails the immediate need for a second defect to regenerate MFI. Although a double defect is required to fully recover the MFI structure, the layers of interpenetrating, dangling silanol groups need not be back-to-back as on the (010) face. Defect density should therefore be significantly lower on the (100) face than on the (010) face.

Such a defecting mechanism is thus capable of accounting for the terraces seen on both the (010) and the (100) faces of both B samples. The relative heights of the terraces would seem to be simply related to the difficulty in overcoming the defect formed. A (010) face defect constitutes a serious barrier to the advancing terraces, requiring a double layer of dangling silanol bonds before the defect can be grown over. This results in the formation of the very high terraces. A (100) face defect also constitutes a barrier to terrace advance; however, this particular defect is more easily grown over, leading to the high terraces.

This mechanism implies a ratio of silanol group defects per unit area on the (010) and (100) facets, respectively, of between 1:1 and 2:1 depending on the degree of MEL growth. Crystal growth sweeps out three distinct volumes as shown in Figure 7. These are the same as the six pairwise correlated sections proposed by Geus et al.[27] Figure 7a depicts overall crystal morphology. Figure 7b depicts the three distinct volume pairs. The {010} facets sweep out the top and bottom pair of volumes, shaded in dark gray, containing the back-to-back double defects. The {100} facets sweep out the front and back pair of volumes, shaded in light gray, containing the disparate double defects separated by MEL structure. In the proposed defecting mechanism, the side pair of volumes, swept out by the {101} and {10$\bar{1}$} facets, should contain no double density defects. AFM imaging of the (101) facet, shown in Figure 8, reveals the existence of poorly defined terraces. Section analysis reveals that these terraces have heights between 30 and 60 nm.

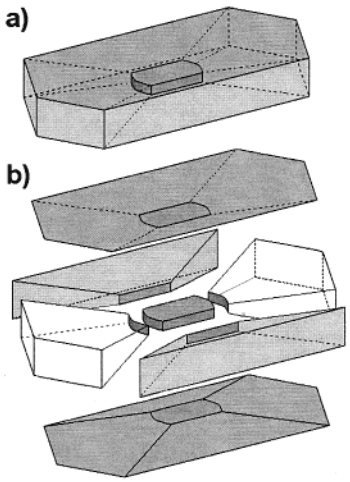

Figure 7. Schematic representation of the volumes swept out by the individual facets of a silicalite crystal during growth. (a) shows the entire crystal, and (b) shows the three separate pairs of sections, shown in dark gray, light gray, and white.

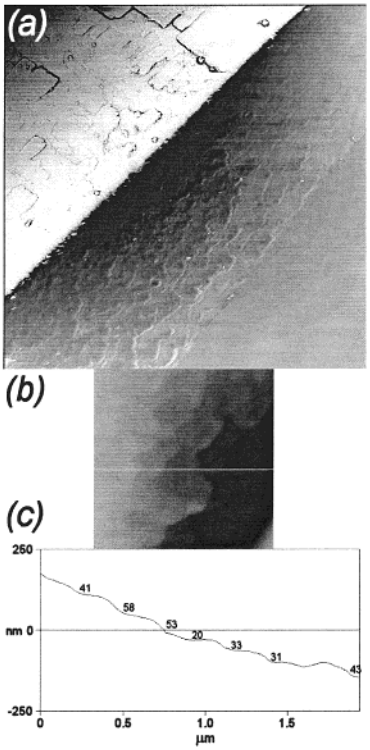

Figure 8. (a) AFM phase image of a (101) face of silicalite sample B1; the light face is the (100) face. (b) 2.0 × 2.0 μm^2 AFM height image of part of the face and (c) the corresponding section analysis taken along the white line.

Table 1. Assignment of Silanol Group Stretches in the FTIR Spectra Shown in Figure 5c

experimental $\tilde{\nu}$/cm^{-1}	literature $\tilde{\nu}$/cm^{-1}	peak assignment
3730	3733	silanol groups free from H-bonding
3691	3680	different structures of terminal silanol groups H-bonded solely through the O atom
3612	3625	
3531	3510	H-bonded silanol groups

FTIR microscopy has been used to explore the existence of these differing crystal volumes in terms of defect density. Both the back-to-back and the disparate defects comprise silanol group chains. The silanol groups within these chains are almost certainly hydrogen bonded because of their proximity. The ultimate aim of differentiating between the two types of silanol chain defects was deemed unlikely. However, focusing the beam at one end of the (010) face and scanning it along the [001] direction should result in changes in the recorded spectrum as the relative quantities of both silanol chain defects rise to maxima at the center of the face and fall to their original minima at the other end.

Figure 5c shows the evolving FTIR spectrum as the spot is tracked from one end of the crystal to the other. The minute aperture severely limits signal-to-noise ratio in these spectra; however, there are two points of note. First, the top spectrum compares well with FTIR spectra recorded on bulk crystals outgassed at similar temperatures. Peak assignments based on detailed studies by Zecchina et al.[29] and Astorino et al.[30] are given in Table 1. The spectrum shows one peak assigned to non-hydrogen bonded silanol groups, two peaks assigned to different structures of terminal silanol groups, hydrogen bonded only through their O atoms, and one broad peak assigned to fully hydrogen bonded silanol groups. Second, and perhaps of greater significance, the spectra recorded from the crystal extremities are similar, but the spectrum changes dramatically passing over the central portion of the face. Although this effect is difficult to quantify, there is a distinct increase in all three signals associated with hydrogen bonded silanol groups. The peak at 3691 cm^{-1} also shifts to a higher wavenumber, thus becoming a shoulder of the non-hydrogen bonded silanol group peak. This increasing abundance of hydrogen bonded silanol groups may be attributed to the volumetric increase in the number of silanol chain defects in support of the proposed defecting mechanism.

The difference in nucleation rates and similarity in terrace spreading rates between the (010) and (100) faces may now be explained. Nucleation on the two faces differs in the symmetry relationship between the fresh nucleus and the existing structure − mirror plane on the (010) face, inversion center on the (100) face. A difference in activation energy of the two attachment processes is therefore not unreasonable. Assuming a 4-fold difference in rate at the synthesis temperature of 130 °C and identical preexponential factors (likely to be governed by nutrient-surface collision rates and similar for both faces in a homogeneous gel), we calculated the difference in activation energy to be 4.6 kJ mol^{-1}. Analogy may be drawn with the zeolite Y polymorphs FAU and EMT.[33] In FAU, successive layers are related via inversion center; in EMT, they are related by mirror plane. Zeolite Y grows more readily as the FAU polymorph − EMT requires a crown ether to force mirror symmetry connectivity.

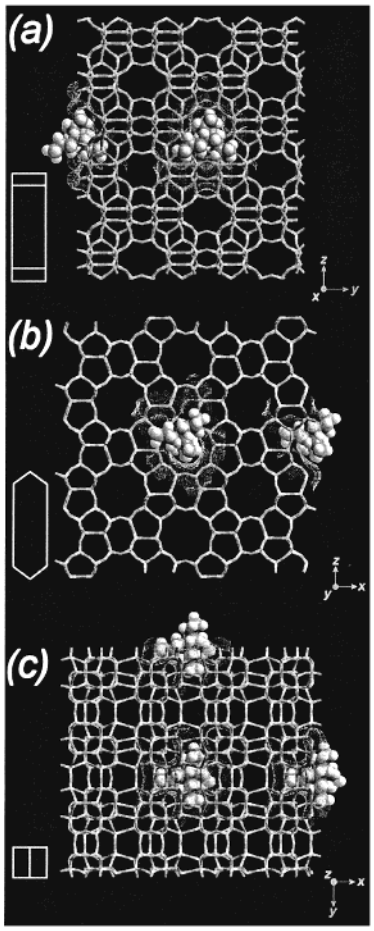

Figure 9. Views down: (a) [100]; (b) [010]; (c) [001] of the structure of MFI, showing the position and orientation of TPA molecules and their associated Connolly surfaces.

Terrace spread occurs at terrace edges and requires connections via both symmetries, regardless of face. On the (010) face, attachment to the underlying surface is via mirror symmetry, and attachment to the edge of the terrace is via inversion symmetry. On the (100) face, the situation is analogous but reversed. This similarity of energetics could explain the similar terrace spreading rates on the two faces.

Templating will also play a crucial role in the energetics of surface attachment in the silicalite system. Tetrapropylammonium cations are known to be located at the intersections of the sinusoidal and straight channels with two propyl arms extending along each.[34] Prior to the formation of a new layer on either face, the template molecules must key into the surface at the channel intersections. The sinusoidal channels open onto the {100} faces, Figure 9a; the straight ones open onto the {010} faces, Figure 9b. Thus, the projecting propyl arms of cations on the two faces will be oriented differently − on {010} they will be normal to the face, and on {100} they will be at an angle, seen most clearly in Figure 9c. This will undoubtedly

(33) Hanif, N.; Anderson, M. W.; Alfredsson, V.; Terasaki, O. *Phys. Chem. Chem. Phys.* **2000**, *2*, 349−357.
(34) Koningsveld, H.; van Bekkum, H.; Jansen, J. C. *Acta Crystallogr.* **1987**, *B43*, 127−132.

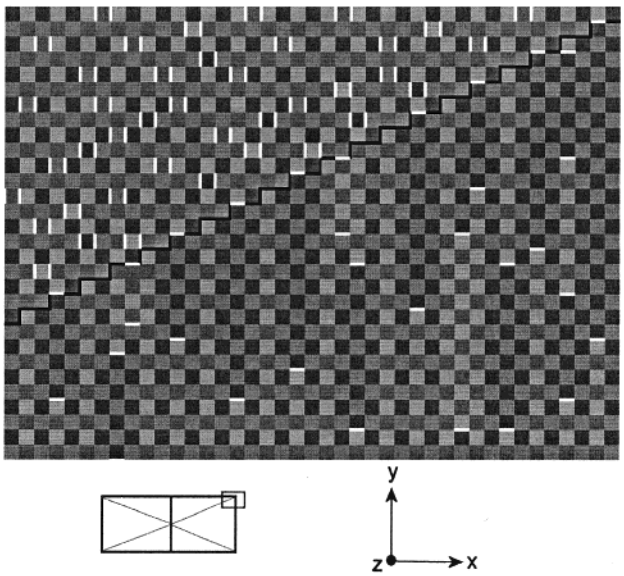

Figure 10. A schematic representation of the growth of silicalite in the vicinity of the interface of the optical hourglass, depicted as the black zigzag line. Location and orientation are given below. Defect chains, comprising interpenetrating silanol groups running along [001], are depicted as white lines.

affect surface attachment and subsequent template clathration. Connolly surfaces, calculated for silicalite atoms within an 8 Å radius of the template nitrogen atoms, are shown. They highlight the close fit between template cations and the microporous structure.

There is debate in the literature concerning both the origin of the hourglass phenomenon, observed by optical microscopy, and the possibility of 90° intergrowths/twinning in silicalite. In 1982, Price et al. studied fluoride silicalite crystals.[25] Weissenberg photographs about the *c* axis (not actually given in the paper) showed pairs of diffractions indicating interpenetrant twinning. High-angle spots were used to show that the *a* direction of one twin component was parallel to the *b* direction of the other and vice versa. Observation of the hourglass phenomenon was attributed to the difference in the double refraction of the twin components.

In 1990, Hay et al. observed the hourglass phenomenon in ZSM-5 crystals and used ultrasonic treatment to dislodge intergrowth components.[26] However, little evidence of 90° intergrowth is given in the paper. The authors claim it was determined from selected area electron diffraction for crystals smaller than 20 μm, although no data are given. For larger crystals, it was deduced from crystal morphology alone. The possibilities of dislodging intergrowths via ultrasonic treatment and the preferential dissolution of twinned crystals along the domain boundaries[35] imply a weakness in the crystal along the interfaces of the hourglass. The defecting mechanism proposed herein affords an explanation for this, based on the crystal schematic given in Figure 10. The schematic, drawn in the style of Figure 6, illustrates a (001) section of growth of a small portion of the crystal, the location of which is given pictorially at the bottom-left of the figure. The black zigzag line represents the hourglass interface boundary. In the volume of the crystal swept out by the (010) face, that is, above the black line, a multitude of back-to-back, double-density defects may be seen, depicted by double white lines. In the volume of the crystal swept out by the (100) face, that is, below the black line, the disparate double-density defects may be seen, depicted by double white lines, separated by extended portions of the MEL structure. This figure highlights two points. First, defect density is clearly much lower in the latter volume because of the possibility of growing the MEL structure. Second, terraces on the (100) face growing as MEL are forced to grow back to MFI at the edge of the face, generating the second half of the double-density defect. This forced occurrence of an otherwise random event creates a very high defect density along the interface leading to the experimentally observed structural weakness. Moreover, this explanation applies equally to planar or curved hourglass interfaces. Interface geometry simply depends on the constancy of the relative nucleation rates on the two faces.

In 1994, Geus et al. reported an optical and IR study of the calcination of silicalite.[27] The single crystal nature of the sample was established by X-ray diffraction on only one silicalite crystal, and, again, no experimental data were provided. An hourglass, with clearly nonlinear interface boundaries, was observed. The authors propose division of the crystal into the same six pairwise correlated sections proposed in the present study (Figure 7). With reference to the paper by Hay et al.,[26] the authors question whether the micropore structure extends over the whole crystal, speculating that the interface might involve weak bonding between different crystal sections and possible pore blocking. This is postulated as a possible cause of the nonuniform degradation of the tetrapropylammonium template during calcination.

Also, in 1994 Weidenthaler et al. reported an optical investigation of intergrowth effects in silicalite.[24] Precession photographs proved that the crystallographic *c* axis lay parallel to the long axis of the crystal. The similarity of photographs taken perpendicular to the two main faces of the crystal seemed to indicate a 4-fold axis along the *c* direction; however, powder XRD revealed orthorhombic symmetry, and thus the authors suggested the crystals were twinned, in agreement with Price et al.[25] However, the authors highlight the danger in drawing such conclusions because of the similarity in *a* and *b* lattice parameters for silicalite. The optical microscopy study shows images of the hourglass phenomenon, and the authors attribute this to the 90° intergrowth nature of the crystals. They consider the crystal to be split into two individuals: one comprises two pyramidal species that interpenetrate the elongated orthorhombic prism that comprises the other. Under crossed polars, the interference colors of the two sections are different, indicative of different refractive indices. Thus, providing the two individuals are chemically and crystallographically identical, then the n_y and n_z axes of the optical indicatrix cannot coincide for the two individuals, providing further proof of 90° intergrowth. However, the difference in refractive indices may simply be attributable to varying chemical composition in the different sectors. Thus, varying silanol group concentrations caused by the creation of defects in the layer growth process of silicalite might be the origin of the hourglass phenomenon. Sample A silicalite crystals, that appear to be nondefected on the basis of their regular terrace topography, should thus not show the optical hourglass phenomenon, and this is the experimental observation. However, the result may simply be attributed to the crystals

(35) Cundy, C. S.; Henty, M. S.; Plaisted, R. J. *Zeolites* **1995**, *15*, 342−352.

being too small for the effect to be detected and thus offers minimal support to the theory.

Employing iodine adsorption and subsequent optical microscopy Kočiřík et al.[36] and Pachtová et al.[37] showed that domain boundaries provide enhanced sorption routes into silicalite crystals. Analysis is based on the assumption of 90° intergrowth; however, the observation might be explained by the high defect presence at these boundaries.

It is noteworthy that the morphology of ZSM-5 and silicalite samples studied in the literature varies. Certain crystals seem flawless; others show clear signs of intergrowth. It is therefore problematic to draw global conclusions. However, the phenomenon of 90° intergrowth implies expression of the same {100} crystallographic facet on all four main faces. It would therefore be expected that the surface structure observed by AFM would be identical on the (010) and (100) faces, which is clearly not the case. The 5-fold difference in terrace heights on the two faces of both B samples is compelling evidence to refute the existence of an intergrowth structure. The hourglass phenomenon is caused by differences in refractive index between various zones of the crystal. Our data suggest such differences are caused by differing silanol group concentrations.

Conclusions

Ostensibly, under certain conditions, silicalite (akin to zeolites A and Y) grows via a layer mechanism − each layer being one pentasil chain high. A constant-area-deposition mechanism, not dominated by addition at kink sites, is evident, and this results in overall circular growth fronts. The aforementioned mechanism is consistent with macroscopic crystal growth kinetics, although future work, intended to clarify the effects of decreasing gel supersaturation toward the end of synthesis, is underway and will be reported elsewhere. It appears likely that "ski-ramp" type features on the (010) surface may indeed be individual 90° intergrowths.

Some synthetic conditions lead to the formation of silicalite crystals with terraces up to 110 nm high on the (010) face and up to 20 nm high on the (100) face. Such terraces bear no relation to any simple structural element of the zeolite. Assumption of a layer growth mechanism leads to the conclusion that an impediment to terrace advance causes a build up of the layers. The defect inclusion mechanism, detailed in this paper, explains how this might occur. The mechanism may be used to explain the relative terrace heights on the two faces and generates the possibility of chemically distinct sectors within the crystal, having different refractive indices that we suggest might be the origin of the often observed hourglass phenomenon.

Acknowledgment. J.R.A. and N.H. gratefully wish to acknowledge the EPSRC for the award of Advanced Fellowship no GR/A90985/01 and for funding under grant no GR/M59365/01, respectively. The authors are indebted to Prof. J. Dwyer for suggesting the IR microscopy and for use of the microscope and to Mr R.J. Plaisted and Dr. S. J. Weigel for preparing silicalite samples A and B1, respectively. We are most grateful to Dr U. Müller for the generous gift of sample B2.

JA020899F

(36) Kočiřík, M.; Kornatowski, J.; Masařík, V.; Novák, P.; Zikánová, A.; Maixner, J. *Microporous Mesoporous Mater*. **1998**, *23*, 295−308.
(37) Pachtová, O.; Kočiřík, M.; Zikánová, A.; Bernauer, B.; Miachon, S.; Dalmon, J.-A. *Microporous Mesoporous Mater*. **2002**, *55*, 285−296.